Vorticity isotropy in high Karlovitz number premixed flames

Brock Bobbitt and Guillaume Blanquart

Citation: Physics of Fluids **28**, 105101 (2016); doi: 10.1063/1.4962305
View online: http://dx.doi.org/10.1063/1.4962305
View Table of Contents: http://scitation.aip.org/content/aip/journal/pof2/28/10?ver=pdfcov
Published by the AIP Publishing

PHYSICS OF FLUIDS **28**, 105101 (2016)

Vorticity isotropy in high Karlovitz number premixed flames

Brock Bobbitt[a] and Guillaume Blanquart
Department of Mechanical Engineering, California Institute of Technology, 1200 E. California Blvd., Pasadena, California 91125, USA

(Received 15 March 2016; accepted 15 August 2016; published online 4 October 2016)

The isotropy of the smallest turbulent scales is investigated in premixed turbulent combustion by analyzing the vorticity vector in a series of high Karlovitz number premixed flame direct numerical simulations. It is found that increasing the Karlovitz number and the ratio of the integral length scale to the flame thickness both reduce the level of anisotropy. By analyzing the vorticity transport equation, it is determined that the vortex stretching term is primarily responsible for the development of any anisotropy. The local dynamics of the vortex stretching term and vorticity resemble that of homogeneous isotropic turbulence to a greater extent at higher Karlovitz numbers. This results in small scale isotropy at sufficiently high Karlovitz numbers and supports a fundamental similarity of the behavior of the smallest turbulent scales throughout the flame and in homogeneous isotropic turbulence. At lower Karlovitz numbers, the vortex stretching term and the vorticity alignment in the strain-rate tensor eigenframe are altered by the flame. The integral length scale has minimal impact on these local dynamics but promotes the effects of the flame to be equal in all directions. The resulting isotropy in vorticity does not reflect a fundamental similarity between the smallest turbulent scales in the flame and in homogeneous isotropic turbulence. *Published by AIP Publishing.* [http://dx.doi.org/10.1063/1.4962305]

I. INTRODUCTION

The three Kolmogorov hypotheses[1] are fundamental to current theory and modeling of homogeneous isotropic turbulence (HIT). These same models are often then applied within premixed turbulent combustion.[2–5] However, it is not clear if all three hypotheses are valid in premixed turbulent combustion, where the density and viscosity vary significantly and the flame introduces specific length and velocity scales. Recently, the validity of Kolmogorov's first similarity hypothesis was addressed in high Karlovitz number (Ka) turbulent premixed flames.[6] It was found that enstrophy, $\Omega = \boldsymbol{\omega} \cdot \boldsymbol{\omega}$, where $\boldsymbol{\omega}$ is the vorticity vector, scales with the inverse of the Kolmogorov time scale, $\Omega \propto 1/\tau_\eta^2$ (which is a function of the dissipation rate, ϵ, and kinematic viscosity, ν, alone) given a sufficiently high Karlovitz number. The current work aims to investigate the isotropy of the small scale turbulence, which relates to Kolmogorov's hypothesis of local isotropy. Investigating the smallest turbulent scales is also particularly important as these scales must be modeled in Large Eddy Simulations (LES)[7,8] and are known to alter the internal structure of the flame.[9–13]

In premixed turbulent combustion, the coupling of the flame and turbulence has been observed to vary with the Karlovitz number.[2,9,13–18] The Karlovitz number is defined as the ratio of the flame time scale (τ_F) to that of the smallest turbulent eddies (τ_η),

$$\mathrm{Ka} = \frac{\tau_F}{\tau_\eta}, \tag{1}$$

where $\tau_\eta \equiv (\nu/\epsilon)^{1/2}$. τ_F is evaluated as $\tau_F = l_F/S_L$ where S_L is the laminar flame speed and l_F is the laminar flame thickness, defined here as $l_F = (T_b - T_u)/|\nabla T|_{max}$. It is common to evaluate the

[a] Author to whom correspondence should be addressed. Electronic mail: bbobbitt@caltech.edu

Karlovitz number using τ_η in the unburnt flow; this quantity is referred to as the unburnt Karlovitz number (Ka_u). The focus of this study is on high Ka premixed flames.

Building on our previous work,[6] the present study focuses on the isotropy of the smallest turbulent scales by considering the vorticity vector. The vorticity vector is chosen as it is characteristic of the smallest turbulent scales[19–21] and comparison of its three components may be used to assess flow isotropy. Additionally, vorticity may be evaluated locally in physical space without the use of Fourier transforms (which require periodicity), and it may be projected onto various coordinate systems, such as the eigenframe of the strain-rate tensor, $S = 1/2(\nabla \boldsymbol{u} + \nabla \boldsymbol{u}^T)$, providing insights into the local flame/turbulence dynamics. Furthermore, vorticity has a known transport equation, and the terms in its transport equation may be readily related to physical processes.

Previous relevant studies on small scale isotropy within premixed flames include those of Hamlington *et al.*,[15,16] Poludnenko,[22] and Lipatnikov *et al.*[23] Lipatnikov *et al.*[23] considered direct numerical simulations (DNSs) at low unburnt Karlovitz numbers ($\mathrm{Ka}_u^* = 0.2$–0.3, where $\mathrm{Ka}_u^* = (l_F/l)^{1/2}(u_o/S_L)^{3/2}$ and l and u_o are the integral length and velocity scales, respectively). They found anisotropy in vorticity and related this primarily to the effects of baroclinic torque. The vortex stretching/production term was found to be unimportant in these low Ka_u^* simulations. Recently, Poludnenko[22] discussed the magnitude of the terms in the vorticity equation for moderately high values of the Karlovitz number ($\mathrm{Ka}_u = 7$–30). These simulations of H_2-air premixed turbulent flames relied on numerical viscosity in an implicit large eddy simulation (ILES) framework.[24] At the lower Karlovitz number tested ($\mathrm{Ka}_u = 7$), the author found that the total production of vorticity was anisotropic, due to the significant role of dilatation and baroclinic torque. However, at the higher value of Ka_u ($\mathrm{Ka}_u = 30$), the total production of vorticity was largely isotropic. The only relevant study at higher Karlovitz numbers is by Hamlington *et al.*[15,16] who performed several DNSs of premixed H_2-air flames varying the turbulence intensity ($\mathrm{Ka}_u^* = 3$–125). These simulations were at a single value of l/l_F and flame density ratio, and once again relied on numerical viscosity using an ILES framework. In their work, they observed that anisotropy decreased as the turbulence intensity increased and offered a possible explanation for anisotropy involving vortex stretching and the local alignment of vorticity and the flame. The effect of baroclinic torque and viscous dissipation on isotropy was not considered in their analysis. In these simulations which rely on an ILES framework, it is not clear how the absence of physical viscosity impacts the development of vorticity anisotropy. This is particularly relevant to consider as it was found that temperature dependent viscosity is central to correctly capturing enstrophy transport through the flame.[6]

Despite these previous contributions, it still remains unclear if and when the smallest turbulent scales are isotropic within the flame. Additionally, it is uncertain what mechanism is responsible for producing small scale anisotropy and how this is impacted by different parameters. Considering the above, the goals of the current study are first to determine if the smallest turbulent scales are isotropic in high Karlovitz number premixed flames; and second, to isolate the process which is primarily responsible for producing small scale anisotropy. The final goal is to determine how different parameters (such as Ka_u and l/l_F) impact small scale anisotropy. These goals are accomplished by analyzing a series of DNS with varying Karlovitz numbers, Reynolds numbers, and flame density ratios previously performed by Bobbitt *et al.*[6] The simulations are of statistically one-dimensional, slightly lean *n*-heptane/air flames using either finite-rate chemistry or tabulated chemistry. Simplified chemical and transport models are often used in numerical simulations of premixed turbulent combustion to reduce the computation cost,[15,16,18,22,23,25] but their impact on vorticity isotropy is not known. By analyzing DNS with different models, their impact on vorticity may be tested.

The paper is organized as follows. In Section II, the physical configuration, governing equations, and numerical approach for the DNS are reviewed. Section III presents an analysis addressing the presence of small scale isotropy followed by an investigation of the vorticity equation to identify the specific term primarily responsible for the production of anisotropy. Section IV then presents a further analysis on the impact of different parameters on anisotropy. Lastly, a discussion of the conclusions and their application is provided in Section V.

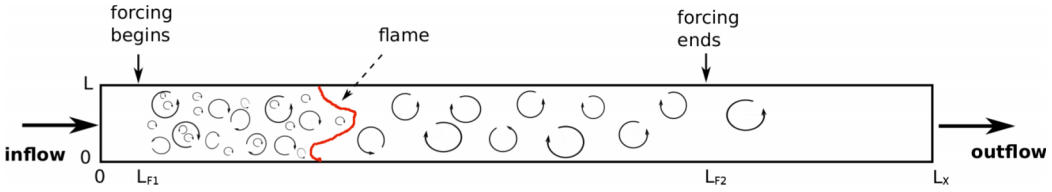

FIG. 1. Computational domain demonstrating the approximate location of the flame and region of forcing. Diagram adapted with permission from B. Savard *et al.*, Proc. Combust. Inst. **35**, 1377 (2015). Copyright 2015 The Combustion Institute.

II. OVERVIEW OF DIRECT NUMERICAL SIMULATIONS

The analysis in this study is based on the recent DNS of high Karlovitz number statistically planar flames by Bobbitt *et al.*[6] The physical and numerical setup of these DNSs are reviewed here briefly. For additional details, the reader is referred to Bobbitt *et al.*[6]

A. Physical configuration

The simulations used for the present analysis are of statistically stationary, statistically planar premixed turbulent *n*-heptane/air flames at a slightly lean equivalence ratio ($\phi = 0.9$) and atmospheric pressure. The three-dimensional domain has an inflow and outflow at the left and right x boundaries, respectively, and periodic boundary conditions in the y and z directions (Fig. 1). The height and width of the channel are equal and denoted as L, while the length is L_x. A separate DNS was performed of relatively weak, homogeneous, isotropic, triply periodic box turbulence and was used to generate the inflow condition. The mean inflow velocity is constant for each case, and is set to a value approximately equal to the turbulent flame speed, allowing for an arbitrary long run-time. This configuration was designed to have no mean shear so that the effects of the flame on the turbulence may be studied in isolation.

All simulations were performed in the work of Bobbitt *et al.*[6] and were originally based on the previous work of Savard *et al.*[11] and Lapointe *et al.*[13] Only cases A, B, $B_{Tab,1}$, $B^4_{Tab,1}$, C^*, and D performed by Bobbitt *et al.*[6] are considered here. All necessary information about the different simulations is provided in Table I. The turbulence intensity, l_o/l_F, and temperature in the reactants vary between simulations to investigate the effects of the unburnt Karlovitz number, integral length scale, and flame density ratio. The unburnt Karlovitz number and turbulent Reynolds number each vary by an order of magnitude ($Ka_u = 70$–750, $Re_{t,u} = 83$–1150) and the unburnt temperature spans

TABLE I. Physical and numerical parameters of the DNS analyzed in the present study. Subscripts 1 and Tab correspond to simulations using unity Lewis numbers and tabulated chemistry, respectively; a superscript of 4 corresponds to $l_o/l_F = 4$. l_o is an estimate of the integral length scales based on the domain size.[26,27] $Re_{t,u} = u'_u l_o/\nu$, u'_u, and η_u are the turbulent Reynolds number, rms velocity fluctuation, and Kolmogorov length scale, respectively, all in the unburnt gas.

	A	B	$B_{Tab,1}$	$B^4_{Tab,1}$	C^*	D
T_u (K)	298	298	298	298	298	800
ρ_u/ρ_b	7.8	7.8	7.8	7.8	7.8	3.3
L_x (mm)	25.6	25.6	25.6	60.6	25.6	16.8
L (mm)	2.33	2.33	2.33	9.32	2.33	1.53
Grid	11×128^3	11×128^3	11×128^3	2574×512^2	11×240^3	11×220^3
L_{F1}	$0.5L$	$0.5L$	$0.5L$	$0.5L$	$0.5L$	$0.5L$
L_{F2}	$8L$	$8L$	$8L$	$4.5L$	$8L$	$8L$
$Re_{t,u}$	83	190	190	1150	390	380
Ka_u	70	220	280	280	640	750
u'_u/S_L	9	18	21	33	37	45
l_o/l_F	1.1	1.1	1.0	4	1.1	1.2
η_u (μm)	16	9	9	9	5.1	3.5
S_L (m/s)	0.36	0.36	0.29	0.29	0.36	2.3
l_F (mm)	0.39	0.39	0.43	0.43	0.39	0.25

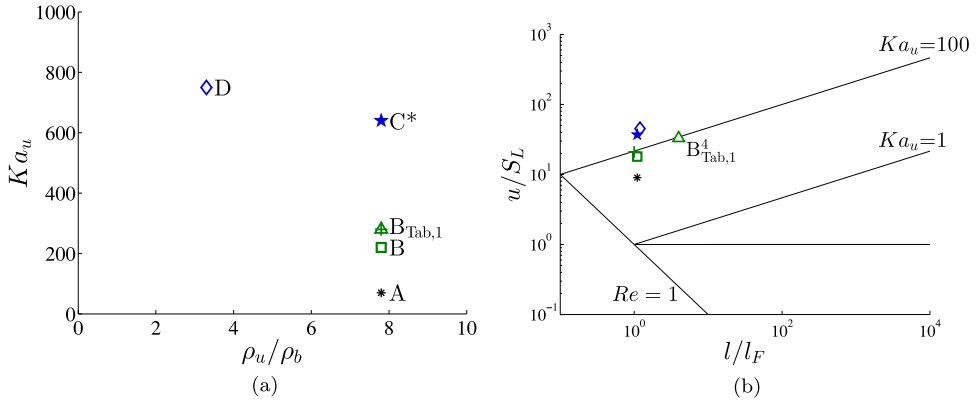

FIG. 2. Conditions in the unburnt flow of the different simulations: (a) Karlovitz numbers and density ratios and (b) Peters regime diagram.[2] Symbols on the left plot correspond to the same simulations on the right.

conditions of relevance to practical engines (T_u = 298–800 K). Cases A, B, and C* have different values of Ka_u but the same flame density ratio. Case $\mathrm{B}^4_{\mathrm{Tab},1}$ has the same Karlovitz number as case B but an integral length scale which is four times larger. Case $\mathrm{B}_{\mathrm{Tab},1}$ has the same conditions as case B, and is provided to test the impact of unity Lewis number transport and tabulated chemistry on the behavior of small scale isotropy. Case D has value of Ka_u near that of C* but a lower flame density ratio. Figure 2 shows Ka_u and the density ratio for each case as well as their location on Peters' regime diagram. These conditions span the transition from the thin to broken/distributed reaction zone regimes.

To ensure a statistical steady-state, each case was run initially for at least 13 eddy turnover times ($\tau_o = k/\epsilon$, where k is the turbulent kinetic energy (TKE)) to remove any initial transient effects. After this period, data were collected for over $25\tau_o$ in order to provide sufficient statistical samples. Due to the larger domain in case $\mathrm{B}^4_{\mathrm{tab},1}$, each data file contains significantly more independent statistical samples; therefore, it was only necessary to collect data over $7\tau_o$ in this case ($\mathrm{B}^4_{\mathrm{tab},1}$ is run slightly longer for this study). During the simulations, data were collected at a constant rate of approximately $0.5\tau_o$. Further specifications of the simulation conditions are listed in Table I.

B. Governing equations

In the DNS, the low-Mach number reacting flow equations were solved,[28,29] which include equations for the conservation of mass, conservation of momentum, species transport, and temperature,

$$\frac{\partial \rho}{\partial t} + \nabla \cdot (\rho \boldsymbol{u}) = 0, \tag{2}$$

$$\frac{\partial \rho \boldsymbol{u}}{\partial t} + \nabla \cdot (\rho \boldsymbol{u} \otimes \boldsymbol{u}) = -\nabla P + \nabla \cdot \tau + \boldsymbol{f}, \tag{3}$$

$$\frac{\partial \rho Y_i}{\partial t} + \nabla \cdot (\rho \boldsymbol{u} Y_i) = -\nabla \cdot \boldsymbol{j}_i + \dot{\omega}_i, \tag{4}$$

$$\frac{\partial \rho T}{\partial t} + \nabla \cdot (\rho \boldsymbol{u} T) = \nabla \cdot (\rho \alpha \nabla T) + \dot{\omega}_T - \frac{1}{c_p} \sum_i c_{p,i} \boldsymbol{j}_i \cdot \nabla T + \frac{\rho \alpha}{c_p} \nabla c_p \cdot \nabla T. \tag{5}$$

In these equations, ρ is the density, $\boldsymbol{u}$ is the velocity vector, P is the hydrodynamic pressure, and $\boldsymbol{f}$ is the forcing term (see Section II C). Bold symbols are used to denote vectors. The viscous stress tensor is defined as

$$\tau = 2\mu \left(S - \frac{1}{3} (\nabla \cdot \boldsymbol{u}) I \right), \tag{6}$$

where μ is the mixture dynamic viscosity, and I is the identity tensor. In the species equations, Y_i is the mass fraction of species i, $\dot{\omega}_i$ is the species chemical source term, and $\boldsymbol{j}_i$ is the species diffusion

mass flux vector defined as

$$\boldsymbol{j}_i = -\rho D_i \frac{Y_i}{X_i} \nabla X_i - \rho Y_i \boldsymbol{u}_c, \tag{7}$$

where $\boldsymbol{u}_c = -\sum D_i \frac{Y_i}{X_i} \nabla X_i$ is the correction velocity X_i is the species mole fraction, and D_i is the species molecular diffusivity. In the temperature equation, T is the temperature, α is the mixture thermal diffusivity, $\dot{\omega}_T$ is the heat source term defined as $\dot{\omega}_T = \frac{-1}{c_p} \sum h_i \dot{\omega}_i$ where $h_i(T)$ is the species enthalpy, $c_{p,i}$ is the species heat capacity, and c_p is the mixture heat capacity. These equations are combined with the ideal gas law as the equation of state, $\rho = P_o W/RT$ with $1/W = \sum Y_i/W_i$. Here, R is the universal gas constant, W_i is the species molecular weight, and P_o is the thermodynamic pressure.

The n-heptane/air chemistry was modeled with a reduced finite-rate chemical model containing 35 species and 217 reactions (forward and backward counted separately).[11,30] Constant non-unity Lewis numbers were employed,[31] and the species Lewis numbers are the same as those listed in the work of Savard and Blanquart.[12] The chemical and transport models were compared against experimental data and numerical results using full transport (mixture-averaged formulation). Good agreement was found for species mass fractions, species chemical source terms, as well as laminar flame speeds across a wide range of equivalence ratios.[12]

The governing equations were solved using the low-Mach number, variable density, reacting flow solver NGA.[32] The time integration of the chemical source term was performed using a recently developed iterative, semi-implicit method which allows numerical time steps limited here only by the convective Courant-Friedrichs-Lewy (CFL), while remaining second-order accurate in time and free of lagging errors.[33] The overall scheme is second-order accurate in space and time while discretely conserving kinetic energy.[32] Scalar transport was performed with the Bounded QUICK scheme, BQUICK.[34,35] The numerical resolution was selected to resolve all relevant physical length scales of the turbulence and flame, given by the criteria $\kappa_{max}\eta > 1.5$[1] (where κ_{max} is the maximum resolved wavenumber) and a minimum of 20 grid points per l_F.[33] The condition $\kappa_{max}\eta > 1.5$ corresponds to recovering 99% of the dissipation, ϵ.[1] Previous work studying the numerical solver, NGA, confirmed that this criterion was sufficient for resolving the velocity field.[32] Furthermore, the smallest turbulent scales increase in size through the flame so that this resolution criterion is further exceeded within and behind the flame. Additional numerical parameters are provided in Table I.

To reduce the computational cost due to the significantly larger domain, flamelet generated manifolds (FGM), often referred to as tabulated chemistry,[36–39] was used in place of finite-rate chemistry for case $B^4_{Tab,1}$. To test the impact of different chemical and transport models on vorticity isotropy, case $B_{Tab,1}$ is compared against case B. In tabulated chemistry, all fluid properties (including the chemical source term) are tabulated as a function of a single progress variable, C. Figure 3 presents instantaneous contour plots of the progress variable from $B_{Tab,1}$ and $B^4_{Tab,1}$. Tabulation was performed with the solution of a 1D unstretched flame using finite-rate chemistry and unity Lewis number transport. The form of the progress variable was chosen as $C = Y_{H_2O} + Y_{H_2} + Y_{CO_2} + Y_{CO}$, as it is able to track the flame evolution through the preheat and reaction zones.[40] The progress variable

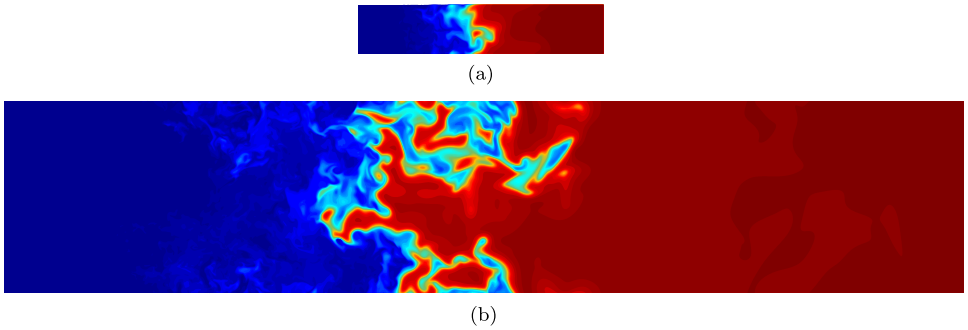

FIG. 3. Two-dimensional slices of C from cases (a) $B_{Tab,1}$ and (b) $B^4_{Tab,1}$. Each figure represents a region of size $L \times 5L$ and both are scaled to match physical length scales.

transport equation is written as

$$\frac{\partial \rho C}{\partial t} + \nabla \cdot (\rho \boldsymbol{u} C) = \nabla \cdot (\rho D \nabla C) + \dot{\omega}. \tag{8}$$

This was used in place of the temperature and species transport equations. The use of tabulated chemistry relaxes the computational cost compared to finite-rate chemistry as a single scalar must be transported. Time integration of the chemical source term was performed explicitly for tabulated chemistry.

C. Turbulence forcing

A variety of configurations have been used in DNS of premixed flames such as V-flames,[41] slot Bunsen flames,[42,43] statistically planar flames with decaying turbulence,[18,44] and statistically planar flames with forced turbulence.[9,10,12,15] In order to isolate the effects of the flame on the turbulence and to reach high Karlovitz numbers, the DNSs analyzed here were statistically planar and used turbulence forcing to prevent the decay of turbulence. Similar methods have been used in the past to investigate both the dynamics of the flame[12,13,45–47] and small scale turbulence.[6,15,16,22] Further analysis and justification of the current configuration were performed by Bobbitt *et al.*[6] The evolution of enstrophy through the flame was in agreement with the unforced, shear-driven, high Karlovitz number slot Bunsen flames of Sankaran *et al.*[43]

In the simulations under consideration, linear forcing, adapted from the work of Carroll and Blanquart,[27] was employed by appending the following term to the momentum equation:

$$\boldsymbol{f} = A \frac{k_o \rho}{k(x,t)} (\boldsymbol{u} - \tilde{\boldsymbol{u}}). \tag{9}$$

Here, A is the forcing parameter equal to $A = 1/(2\tau_o)$, k_o is the target TKE given by $k_o = (27/2) l_o^2 A^2$, and $k(x,t)$ is the instantaneous Favre y-z planar averaged TKE, defined as $k(x,t) = \widetilde{\boldsymbol{u}'' \cdot \boldsymbol{u}''}/2$. The planar Favre average for an arbitrary field ψ is defined as $\tilde{\psi} = \overline{(\rho\psi)}/\overline{\rho}$ with $\psi'' = \psi - \tilde{\psi}$ where $\overline{\psi}$ here is the standard planar average,

$$\overline{\psi}(x,t) = \frac{1}{L_y L_z} \int \psi(x,y,z,t) dy\, dz. \tag{10}$$

In order to avoid negative velocities at the inflow and outflow, forcing was not applied near these boundaries, but only within the range L_{F1} to L_{F2}, which are specified in Fig. 1 and Table I. L_{F1} was chosen so that multiple integral length scales exist between the inflow and the location where forcing begins. L_{F2} was chosen so that sufficient time is given for the turbulence to decay before reaching the outflow.

D. Conditional averaging

Turbulence quantities are expected to vary through the flame based upon the local thermodynamic properties of the fluid (such as density and viscosity). Therefore, in a curved and transient flame, a flame progress variable is preferred over the spatial coordinate x to illustrate progress through the flame. For this reason, averages are conditioned on C, performed over space and time, and denoted as

$$\langle \psi | C \rangle, \tag{11}$$

for a given field ψ. As each fluid property (especially density) correlates very strongly with C, Reynolds and Favre averages are virtually identical in C space.[6] The progress variable is normalized by considering $\hat{C} = C/C_{max}$ so that 0 represents the reactants and 1 represents the products. Conditional averages only include the region where the turbulence forcing is active.

Using this conditional averaging, we define the local Kolmogorov time scale as

$$\tau_\eta(C) = \left(\frac{\langle \nu | C \rangle}{\langle \epsilon | C \rangle} \right)^{1/2}, \tag{12}$$

the local Karlovitz number as $\mathrm{Ka}(C) = \tau_F/\tau_\eta(C)$, and the dissipation rate conditioned on C as $\langle\epsilon|C\rangle = \langle\tau' : S''|C\rangle/\langle\rho|C\rangle$. Additionally, we define a quantity involving the flame density change, $\gamma(C) = \Delta\rho/\langle\rho|C\rangle$, where $\Delta\rho = \rho_u - \rho_b$, which will be used in the subsequent analysis. Further references to these quantities are written as τ_η, γ, and Ka, where the dependence on C is implied.

III. VORTICITY ISOTROPY

In this section, the presence of small scale isotropy is investigated in the high Karlovitz number premixed flames. The vorticity transport equation is then analyzed to isolate the term (or terms) primarily responsible for the production of anisotropy.

A. Isotropy

If the smallest turbulent scales are isotropic, then the vorticity vector components are statistically equal in a fixed Galilean coordinate system. As the present configuration is statistically one-dimensional in x and periodic in y and z, an orthogonal coordinate system aligned with x best characterizes any anisotropy resulting from the flame. Furthermore, as a result of the symmetry of the boundary conditions and governing equations in the y and z directions, any differences between the two corresponding vector components would be due to statistical uncertainty.

Using this domain fixed coordinate system, isotropy of the vorticity vector is assessed by considering a vector, $\boldsymbol{W}$, defined here as the square of each vorticity component less one-third of the enstrophy,

$$W_i = \omega_i^2 - \frac{\Omega}{3}. \tag{13}$$

Subsequently, $\boldsymbol{W}$ will be referred to as the anisotropy vector. Figure 4 presents W_x conditionally averaged on the progress variable. Once again, any deviations from zero are signs of anisotropy. Only the x component is shown as $\langle W_y|C\rangle$ and $\langle W_z|C\rangle$ are equal to $-\langle W_x|C\rangle/2$.

Near the reactants ($\hat{C} \simeq 0$), vorticity is isotropic for all flames. This is simply because the reactants are initialized with homogeneous isotropic turbulence. Consider first cases A, B, and C* (Fig. 4(a)). As the turbulence enters the preheat zone, anisotropy begins to develop in case A, and to a lesser extent in case B. The anisotropy is characterized by a larger vorticity in the direction of the mean flow (x direction) than in the plane of the time-averaged flame (y and z directions). The degree of anisotropy in both cases continues to increase toward the products. In case C*, discernible

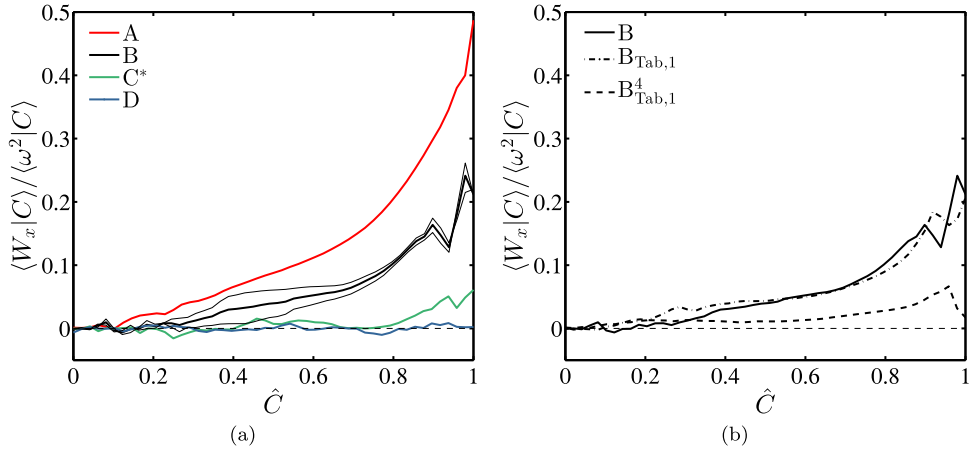

FIG. 4. The anisotropy vector in the x direction, W_x, for cases (a) A, B, C*, and D, as well as (b) B, $B_{Tab,1}$, $B^4_{Tab,1}$. Dashed line at zero represents perfect isotropy. W_x is normalized by the conditionally averaged enstrophy. In (a), thin black lines correspond to averages for case B when either the first or second half of the data is used; they are indicative of the statistical uncertainty in the computed averages.

levels of anisotropy only develop later in the flame. Finally, for case D, with a similar Ka_u but lower flame density ratio compared to case C*, the anisotropy is negligible throughout the flame.

Between cases A, B, and C*, the unburnt Karlovitz number increases by an order of magnitude, yet the ratio of the integral length scale to flame thickness remains close to unity. In contrast, cases B and $\mathrm{B}^4_{\mathrm{Tab},1}$ have the same Karlovitz number but different integral length scales ($l_o/l_F = 1$ and 4, respectively). Equivalently, they also have different turbulent Reynolds numbers ($\mathrm{Re}_{t,u} = 190$ and 1150, respectively) since the Karlovitz number, turbulent Reynolds number, and length scale ratio are not independent,

$$\mathrm{Re}_{t,u} = \left(\frac{l}{l_F}\right)^{4/3} (\mathrm{Ka}^*_u)^{2/3}. \tag{14}$$

As shown in Fig. 4(b), the vorticity in $\mathrm{B}^4_{\mathrm{Tab},1}$ is more isotropic than case B throughout the flame. (Note that there is very good agreement between cases B and $\mathrm{B}_{\mathrm{Tab},1}$, supporting the independence of the observed behavior from the chemical and transport model.)

In summary, at a sufficiently large Karlovitz number and l/l_F, the smallest turbulent scales are found to be isotropic, as defined by Eq. (13). Additionally, isotropy is promoted by lower flame density ratios. This is exemplified in case D, which shows no anisotropy throughout the flame. The dependence of small scale anisotropy on the large turbulent scales is somewhat surprising given they were found to have virtually no impact on the enstrophy.[6] The impact of these parameters on the anisotropy will be further discussed in Section IV.

Hamlington *et al.*[15] observed that the probability density function (PDF) of the vorticity component in the mean flow direction (x direction) resembled isotropic conditions at large turbulence intensities (defined as u'/S_L). Their results are consistent with the decreasing vorticity anisotropy as observed in Fig. 4(a) with increasing Ka_u. However, Hamlington *et al.*[15] observed the onset of isotropy at significantly lower Karlovitz numbers than in the current study. Considering similar density ratios, their case F4 ($\mathrm{Ka}_u = 57$, calculated assuming $\mathrm{Sc} = 1$, where $\mathrm{Sc} = \nu/D$) demonstrated negligible anisotropy, while the present case B ($\mathrm{Ka}_u = 220$) has significant anisotropy. The reason for this difference is addressed in Section V.

B. Source of anisotropy

The source of anisotropy is determined by considering the transport equation for vorticity derived from the momentum equation,

$$\frac{D\boldsymbol{\omega}}{Dt} = S\cdot\boldsymbol{\omega} - \boldsymbol{\omega}\,(\nabla\cdot\boldsymbol{u}) + \frac{1}{\rho^2}(\nabla\rho\times\nabla P) + \nabla\times\left(\frac{1}{\rho}\nabla\cdot\tau\right) + \nabla\times\frac{\boldsymbol{f}}{\rho}, \tag{15}$$

where D/Dt is the material or total derivative. Equation (15) represents a set of three equations, one for each component of the vorticity vector. Each term on the right hand side is associated with a specific physical process: production/vortex stretching, dilatation, baroclinic torque, viscous dissipation, and forcing, respectively. Vortex stretching, viscous dissipation, and forcing are active even when density is constant, while dilatation and baroclinic torque arise here only due to the presence of the flame. The enstrophy transport equation is obtained by taking the dot product of vorticity with this set of equations.

From Eq. (15), we derive the transport equation for the anisotropy vector, $\boldsymbol{W}$. This is accomplished by multiplying each component of the vorticity transport equation by its respective vorticity component, then subtracting one-third of the enstrophy transport equation and grouping corresponding terms,

$$\frac{1}{2}\frac{D\boldsymbol{W}}{Dt} = \boldsymbol{T}_1 + \boldsymbol{T}_2 + \boldsymbol{T}_3 + \boldsymbol{T}_4 + \boldsymbol{T}_5. \tag{16}$$

Terms are again ordered as in Eq. (15) and the explicit form of each is provided in the Appendix. In the remainder of this work, these terms will be referred to as the anisotropic transport terms. For example, $T_{1,x}$ is the anisotropic vortex stretching term in the x direction. To disrupt the base

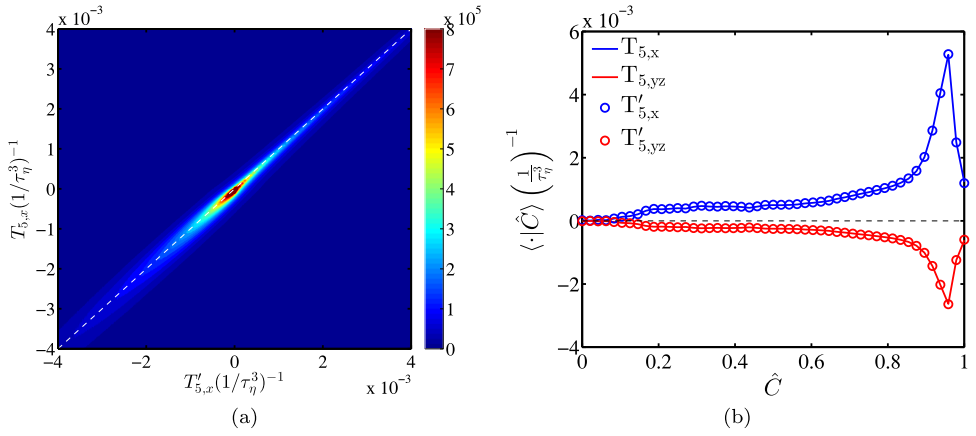

FIG. 5. Comparison of exact versus approximate anisotropic forcing term for case $B^4_{Tab,1}$ through the (a) joint PDF at $\hat{C} = 0.75$ and (b) conditional average of $T_{5,x}$ and $T'_{5,x}$. Both quantities are normalized by $1/\tau_\eta^3$. In (a) the dashed line represents perfect equality between $T_{5,x}$ and $T'_{5,x}$, and in (b) the dashed line at zero represents no anisotropy production.

isotropic flow, the flame must alter the behavior of at least one term in Eq. (16) in order to produce anisotropy. The flame directly alters these terms through changes in the velocity divergence, fluid properties (such as ρ and μ), and mean gradients of turbulence quantities (such as the mean velocity). The dilatation and forcing terms are addressed first.

The anisotropic dilatation term may be written analytically as

$$\boldsymbol{T}_2 = (-\boldsymbol{W})(\nabla \cdot \boldsymbol{u}). \tag{17}$$

In other words, this term is a function of the velocity divergence and depends linearly on $\boldsymbol{W}$. In the absence of anisotropy, this term is identically zero. Thus, this term cannot be responsible for the initial production of vorticity anisotropy. Furthermore, dilatation is expected to decrease the magnitude of $\boldsymbol{W}$ since fluid expansion from heat release results in a positive divergence of velocity. In conclusion, this term cannot initiate or increase anisotropy and will not be further considered as the possible source of anisotropy.

By neglecting gradients of the TKE and mean velocity (i.e., the associated effects of the flame), the forcing term is approximated by

$$\boldsymbol{T}'_5 = A\frac{k_o}{k}\boldsymbol{W}. \tag{18}$$

If the effects of the flame on the forcing term are small, then $\boldsymbol{T}'_5$ well approximates $\boldsymbol{T}_5$. These quantities are compared by computing the joint PDF of the instantaneous, point-wise values of $T_{5,x}$ versus $T'_{5,x}$ for case $B^4_{Tab,1}$ within the flame ($\hat{C} = 0.75$). As shown in Fig. 5(a), the effect of the flame on this term is very small locally and instantaneously. Additionally, Fig. 5(b) shows that on average, the effects of the flame introduce a negligible contribution to the value of anisotropic forcing ($\boldsymbol{T}_5$). Similar results are found for the remaining cases. As the effects of the flame on the anisotropic forcing term are negligible, we approximate $\boldsymbol{T}_5$ as $\boldsymbol{T}'_5$. As with dilatation, this term depends linearly on $\boldsymbol{W}$ and is exactly zero when vorticity is isotropic. Therefore, the growth of anisotropy is not caused by this term, and it will not be further considered.

By exclusion of $\boldsymbol{T}_2$ and $\boldsymbol{T}_5$, either the vortex stretching, baroclinic torque, or dissipation terms must be responsible for the development of vorticity anisotropy. To isolate the cause, their relative contribution to the development of anisotropy is investigated subsequently by considering the effect of the flame on each.

C. Possible sources of anisotropy

The effects of the flame on vortex stretching are isolated by considering $\boldsymbol{T}_1 = \boldsymbol{T}'_1 + \boldsymbol{T}^F_1$, similar to the forcing term, where the effects of the flame are associated with $\boldsymbol{T}^F_1$. In the absence of the

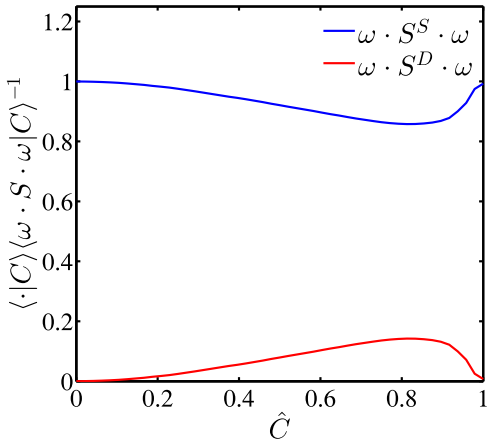

FIG. 6. Dilatational and solenoidal parts of the vortex stretching term in the enstrophy transport equation ($\boldsymbol{\omega} \cdot S^D \cdot \boldsymbol{\omega}$ and $\boldsymbol{\omega} \cdot S^S \cdot \boldsymbol{\omega}$, respectively) for case $B^4_{\text{Tab},1}$. Each is normalized by the vortex stretching term using the full velocity field, $\boldsymbol{\omega} \cdot S \cdot \boldsymbol{\omega}$.

flame, $\boldsymbol{T}_1 = \boldsymbol{T}_1'$. The flame may alter the anisotropic vortex stretching term through the strain-rate tensor (S). The flame-induced flow strain is isolated by performing a Helmholtz (or Weyl) decomposition of the velocity field, $\boldsymbol{u} = \boldsymbol{u}^D + \boldsymbol{u}^S$. For three-dimensional vector fields, there exists a decomposition which separates the vector field into an irrotational component ($\boldsymbol{u}^D$) and a divergence free component ($\boldsymbol{u}^S$), where $\boldsymbol{u}^D = \nabla\phi$ and $\boldsymbol{u}^S = \nabla \times \boldsymbol{B}$. Here ϕ is a scalar potential and $\boldsymbol{B}$ is a vector potential. As a result,

$$\nabla \cdot \boldsymbol{u}^S = 0, \qquad \nabla \cdot \boldsymbol{u}^D = \nabla \cdot \boldsymbol{u},$$
$$\nabla \times \boldsymbol{u}^S = \boldsymbol{\omega}, \qquad \nabla \times \boldsymbol{u}^D = 0.$$

This decomposition is used to separate the strain-rate tensor into that resulting from the dilatational velocity field (S^D) and the solenoidal velocity field (S^S). Under the current low-Mach conditions, dilatation is due only to the heat release and $\boldsymbol{\omega} \cdot S^D \cdot \boldsymbol{\omega}$ can be associated with the effects of the flame in the enstrophy transport equation. The two terms employing the separate velocity fields are plotted for case $B^4_{\text{tab},1}$ in Fig. 6. As expected, $\boldsymbol{\omega} \cdot S^D \cdot \boldsymbol{\omega}$ is non-zero within the flame, while going to zero in the reactants and products where $\boldsymbol{\omega} \cdot S^S \cdot \boldsymbol{\omega}$ is equal to the full term, $\boldsymbol{\omega} \cdot S \cdot \boldsymbol{\omega}$.

This decomposition is applied to the anisotropic vortex stretching term, so that $\boldsymbol{T}_1^D$ and $\boldsymbol{T}_1^S$ employ the strain-rate tensor calculated using only the dilatational and solenoidal velocity fields, respectively. $\boldsymbol{T}_1^D$ is associated with the effects of the flame and, as such, is subsequently referred to as $\boldsymbol{T}_1^F$. The x components of these terms are plotted in Fig. 7(a) for case A. Like the anisotropy vector ($\boldsymbol{W}$), $\boldsymbol{T}_1^F$ is positive in the x-direction. Additionally, the qualitative behavior as a function of $\hat{C}$ is very similar to $\boldsymbol{W}$, with the magnitude increasing through the flame. In contrast, $T^S_{1,x}$ is negative and has the opposite sign as W_x; behavior similar to case A is found in the remaining cases. This suggests that $T^S_{1,x}$ acts to relax the flow to isotropy. In the absence of the flame, the turbulence relaxes the small scales toward isotropy. $T^F_{1,x}$ is provided in Fig. 7(b) for cases A, B, $B^4_{\text{Tab},1}$, C*, and D; and it decreases in magnitude as both the Karlovitz number and l/l_F increase (Fig. 7(b)). From these results, the effects of the flame on the vortex stretching term must be considered as the possible cause for anisotropy.

Lastly, baroclinic torque and viscous dissipation are considered. Baroclinic torque is non-zero only due to the presence of the flame and the induced density gradient. It was observed to contribute significantly to vorticity anisotropy at low values of Ka_u.[23] The effects of the flame on viscous dissipation are determined by, again, separating the flame contribution as $\boldsymbol{T}_4 = \boldsymbol{T}_4' + \boldsymbol{T}_4^F$, where

$$\boldsymbol{T}'_{4,j} = \nu\omega_j\nabla^2\omega_j - \frac{1}{3}\sum_{i=1}^{3}\nu\omega_i\nabla^2\omega_i \tag{19}$$

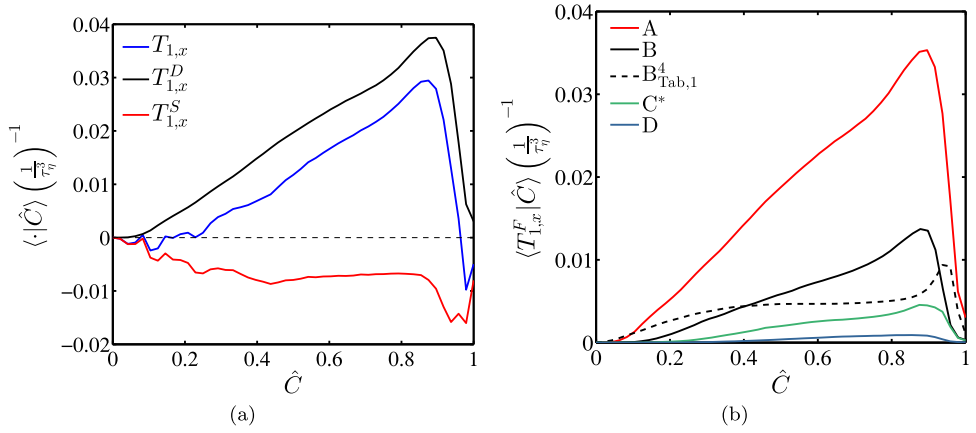

FIG. 7. (a) Anisotropic vortex stretching term ($T_{1,x}$) along with the dilatational ($T^F_{1,x}$) and solenoidal ($T^S_{1,x}$) parts for case A. Dashed line at zero represents no anisotropy production. (b) $T^F_{1,x}$ for cases A, B, $B^4_{tab,1}$, C*, and D.

(summation over repeated indices is not implied). The $\boldsymbol{T}^F_4$ term includes gradients of fluid properties and the velocity divergence.

D. Summary

The contribution of $T^F_{1,x}$, $T_{3,x}$, and $T^F_{4,x}$ to the growth of anisotropy is compared in Fig. 8 for cases A and $B^4_{Tab,1}$. As shown, effect of the flame on the anisotropic vortex stretching term is greater than for both the baroclinic torque and viscous dissipation terms. In all the remaining cases, the magnitude of $T^F_{1,x}$ is larger than $T_{3,x}$ and $T^F_{4,x}$ to a similar or greater extent than in case A.

From these results, it is concluded that the effect of the flame on the vortex stretching term is the primary cause for the growth of anisotropy. As these effects are through the velocity divergence, which may be equated to $-(D\rho/Dt)/\rho$, the anisotropy is a result of the density change through the flame. Sec. IV investigates the impact of the Karlovitz number and l/l_F on the vorticity anisotropy.

IV. LOCAL VERSUS GLOBAL EFFECTS

The purpose of this section is to address how the parameters Ka and l/l_F impact the behavior of the anisotropic vortex stretching term and vorticity vector. This is accomplished by distinguishing aspects of the local flame-turbulence dynamics from the flame geometry and its orientation.

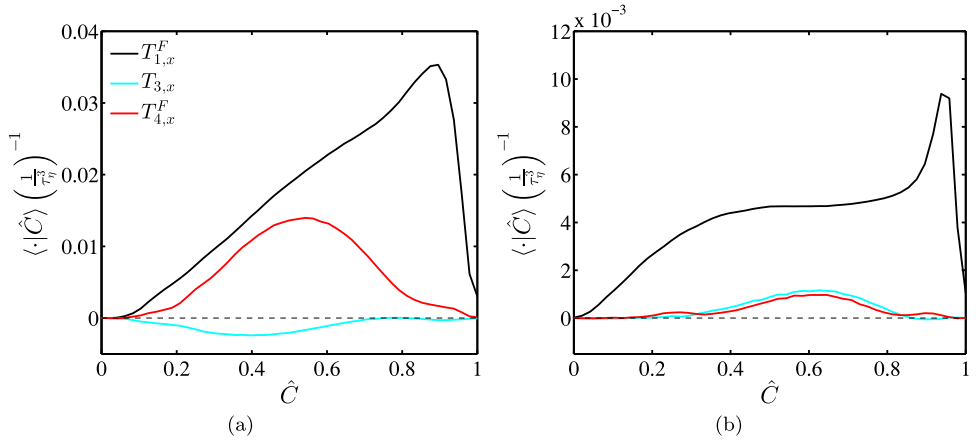

FIG. 8. Terms $T^F_{1,x}$, $T_{3,x}$, and $T^F_{4,x}$ for case (a) A and (b) $B^4_{Tab,1}$, showing the contribution to anisotropy by the effect of the flame on the anisotropic vortex stretching, baroclinic torque, and viscous dissipation terms.

A. Local vorticity behavior

In this section, the local behavior of the vorticity vector is investigated by considering its alignment within the strain-rate tensor, S, eigenframe.[48,49] This is considered because of the importance of this vorticity alignment to the vortex stretching term and the local dynamics of homogeneous isotropic turbulence.[50–53]

1. Review of homogeneous isotropic turbulence

As S is a real symmetric tensor, its eigenvectors are orthogonal and all the eigenvalues are real. The eigenvectors of the strain-rate tensor are denoted as S_1, S_2, S_3 with corresponding eigenvalues, λ_1, λ_2, λ_3. The eigenvalues are listed in decreasing order so that S_1 is the most extensive direction and S_3 is the most compressive direction. Considering DNS of homogeneous isotropic turbulence, Ashurst *et al.*[51] found that vorticity preferentially aligns with the second, or intermediate, eigenvector of the strain-rate tensor (S_2), with a slight preference to align with the S_1 over the S_3 eigenvector. This preferential alignment of vorticity within the eigenframe is often used for gaining insight into the local turbulence dynamics and for modeling purposes.[54] It was also found that λ_2 is, on average, positive, and λ_1 and λ_3 are nearly equal in magnitude but of opposite sign.[50,51] Finally, vortex stretching (represented in the vortex stretching term) is the amplification of vorticity through its alignment with the S eigenvectors that have positive eigenvalues. Therefore, vortex stretching can only occur if vorticity is aligned in either the S_1 or S_2 directions.[50]

2. High Karlovitz number case

The alignment of vorticity with the eigenvectors is discussed first for case D, which is the least anisotropic case, as it has the highest Karlovitz number and lowest flame density ratio. This is investigated qualitatively by computing three-dimensional surface PDFs, referred to here as spherical PDFs. Color levels represent the PDF of the vector orientation and are normalized by the value corresponding to uniform random vector orientation.[54] Spherical PDFs have been previously used as an effective means of communicating the alignment of vorticity in the strain-rate eigenframe.[48,49,54] Figure 9 presents the spherical PDFs of the vorticity alignment for case D near the reactants ($\hat{C} = 0.05$) and within the flame ($\hat{C} = 0.8$). The location $\hat{C} \simeq 0.8$ represents the approximate rear boundary of the turbulent flame brush. By analyzing the data at this location, the extent of the impact of the flame on the turbulence may be seen. These results show the preference for vorticity to align with the S_2 direction, as expected from homogeneous isotropic turbulence.

Results are compared quantitatively with a previous DNS of homogeneous isotropic turbulence by Carroll *et al.*[55] ($\mathrm{Re}_t = 201$; $\mathrm{Re}_\lambda = 55$). This condition is comparable to the turbulent Reynolds number for case D ($\mathrm{Re}_{t,u} = 380$, which reduces to $\mathrm{Re}_{t,b} = 68$ in the products). Comparison is made through the PDFs of $|\cos(\theta_i)|$, where θ_i is the angle between the vorticity vector and the eigenvector S_i, as similarly calculated in previous studies[17,51] (Fig. 10). The alignment of the vorticity vector

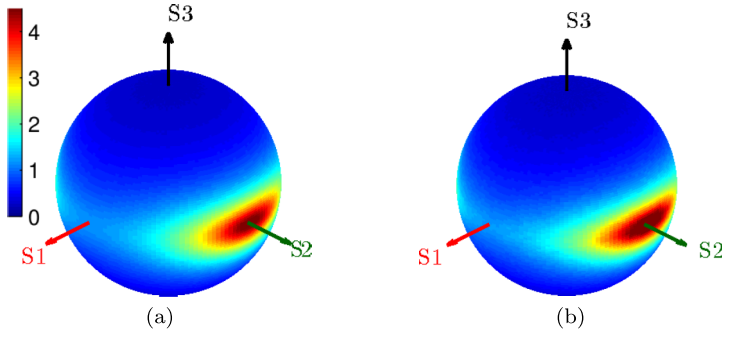

FIG. 9. Spherical PDF for the alignment of vorticity with the S eigenvectors for case D (a) in the reactants ($\hat{C} = 0.05$) and (b) within the flame ($\hat{C} = 0.8$).

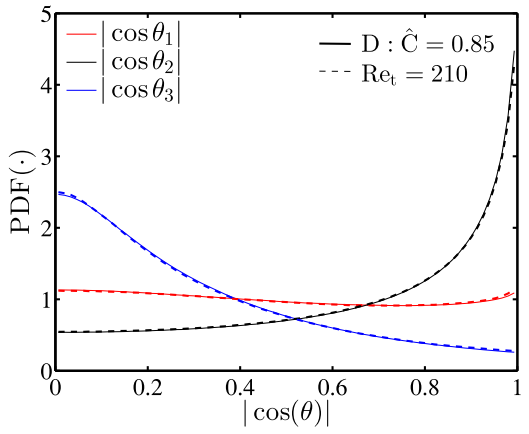

FIG. 10. PDFs of $|\cos(\theta_i)|$ where θ_i is the angle between the vorticity vector and the eigenvector S_i. Solid lines correspond to case D at $\hat{C} = 0.85$. Dashed lines representing $Re_t = 201$ are calculated from the previous simulation of homogeneous, isotropic turbulence by Carroll *et al.*[55]

within the flame is in excellent agreement with results from homogeneous isotropic turbulence. Combined with the vorticity isotropy found in Section III, these results support that given a sufficiently high Karlovitz number, the vorticity isotropy and its alignment within the S eigenframe are unaltered by the flame and resemble that of homogeneous isotropic turbulence.

3. Moderate Karlovitz number cases

In the remaining cases, spherical PDFs (Fig. 11) show that the alignment of vorticity within the S eigenframe is altered by the flame. Qualitatively, there is greater alignment with the S_1 eigenvector, and this change is more prominent at lower values of Ka. Notably, the spherical PDFs of cases B and $B^4_{Tab,1}$ show a similar increase in the alignment with S_1.

Quantitatively, the PDFs of $|\cos(\theta_i)|$ in Fig. 12 similarly show that the alignment with the S_1 direction increases, while the alignment with the S_2 direction decreases in the flame. This result agrees with previous findings in turbulent reacting flows.[15,17,56] To further compare the increased alignment with S_1 between the different cases, the mean value of $|\cos(\theta_1)|$ at $\hat{C} = 0.85$ is plotted versus the corresponding value of Ka/γ (Fig. 13). The quantity Ka/γ was shown previously to capture the competing effects of the turbulence and the velocity divergence on the strain-rate tensor[6] and appears to present a good scaling for the vorticity alignment in the present cases. Once again, cases B and $B^4_{Tab,1}$ are very similar, suggesting the independence of the local vorticity behavior from l/l_F.

As the alignment with the S_1 direction increases at lower Karlovitz numbers, the effects of the flame are to promote an increase in vortex stretching in this direction (S_1 has a positive eigenvalue). This additional production of vorticity by vortex stretching in a manner unlike homogeneous isotropic turbulence is consistent with a growth of anisotropy.

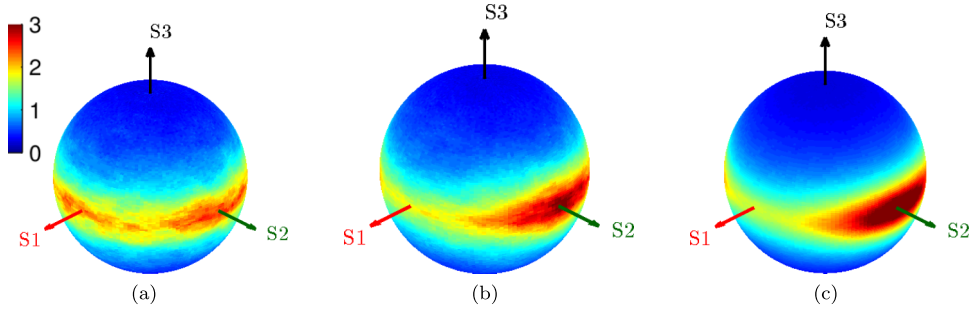

FIG. 11. Spherical PDFs of the vorticity alignment with the strain-rate tensor eigenvectors for case (a) A, (b) B, and (c) $B^4_{Tab,1}$ at $\hat{C} = 0.8$.

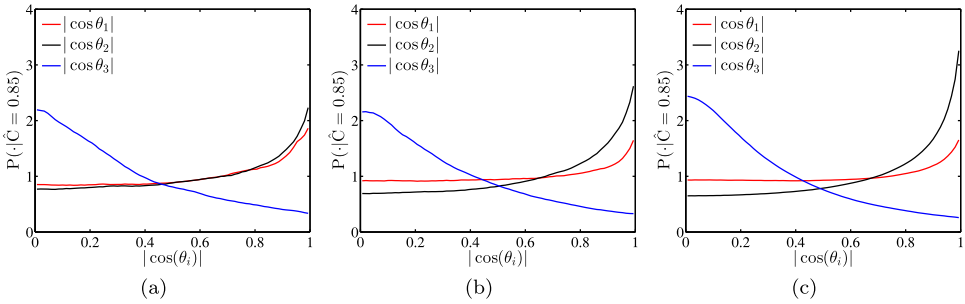

FIG. 12. PDFs of $|\cos(\theta_i)|$ where θ_i is the angle between the vorticity vector and the eigenvector S_i: cases (a) A, (b) B, and (c) $B^4_{tab,1}$ at $\hat{C}=0.85$.

Sec. IV B further investigates the local turbulence behavior by considering the vortex stretching term, due to its importance in generating anisotropy.

B. Local vortex stretching term

The local dynamics of the vortex stretching term are investigated by considering the scalar quantity $\boldsymbol{T}_1^F \cdot \boldsymbol{T}_1^F$, as it is independent of the vector orientation. The purpose of considering this quantity is to remove any dependence on the geometry and coordinate system. A value of zero signifies that the flame does not contribute to anisotropy through this term. Figure 14 shows, as expected, that this quantity is reduced as the Karlovitz number increases and the density ratio decreases. In case D, the effect of the flame on the anisotropic vortex stretching term is smallest.

Notably, there is good agreement between cases B and $B^4_{Tab,1}$. This agreement points to the similar behavior of the anisotropic vortex stretching term in a local sense based on the Karlovitz number and flame density ratio, independent of the flame geometry and large turbulent length scales (l/l_F). Combined with Sec. IV A, these results suggest that the fundamental flame-turbulence interaction is largely unaltered between cases B and $B^4_{Tab,1}$. The cause for the differences of $\langle T^F_{1,x}|C\rangle$ and $\langle W_x|C\rangle$ between cases B and $B^4_{Tab,1}$ (Figs. 4(b) and 7(b)) is investigated next by considering the impact of the large scales through the flame geometry.

C. Flame orientation

The net contribution to anisotropy by $\boldsymbol{T}_1^F$ may be zero ($\langle T^F_{1,i}|C\rangle = 0$), even if $\boldsymbol{T}_1^F$ is locally and instantaneously non-zero. This occurs if the flame alters the vortex stretching term but does so equally

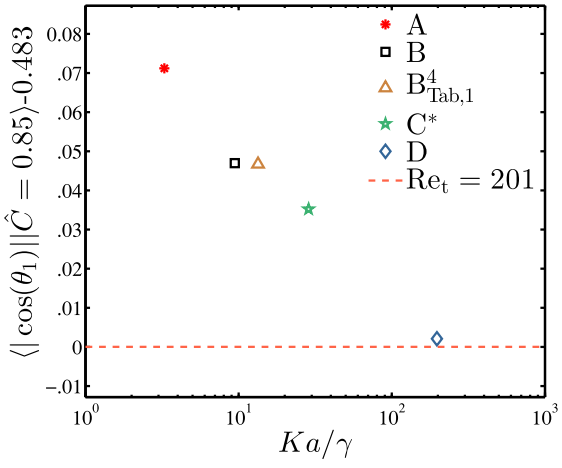

FIG. 13. Mean value of $|\cos(\theta_1)|$ at $\hat{C}=0.85$, showing the increased alignment with the S_1 eigenvector as a function of Ka/γ (also evaluated at $\hat{C}=0.85$). Values are relative to that of homogeneous, isotropic turbulence at $Re_t=201$, calculated from the DNS previously preformed by Carroll *et al.*[55] and represented by the dashed line at zero.

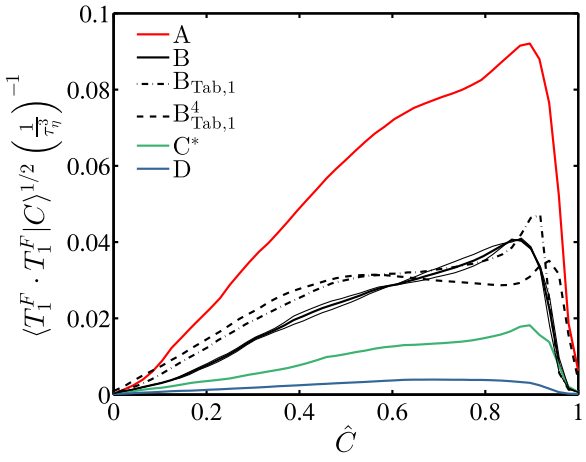

FIG. 14. Conditional average of $\boldsymbol{T}_1^F \cdot \boldsymbol{T}_1^F$ for cases A, B, $B_{Tab,1}$, $B^4_{Tab,1}$, and D. Thin black lines correspond to averages for case B when either the first or second half of the data is used; they are indicative of the statistical uncertainty in the computed averages.

in all directions. This geometric effect is particularly relevant due to this term's dependence on the dilatational velocity field, $\boldsymbol{u}^D$, which depends on the flame geometry through the density field. This is illustrated in Fig. 15 by considering two hypothetical cases with different flame geometries. In this figure, the solid black line represents the surface of the flame and the arrows represent the effect of the flame on vorticity. As shown, even if the local behavior is similar along the flame surface, differences in a fixed coordinate system cause the net contribution to anisotropy to not be equal.

As a measure of the flame surface orientation, Fig. 16 presents the PDFs of $(\partial\rho/\partial x)/|\nabla\rho|$ within the flame ($\hat{C} = 0.85$). For all cases, the density gradient is on average in the x direction, corresponding to a value of $(\partial\rho/\partial x)/|\nabla\rho| = 1$. Departure of the PDFs from this alignment is due to wrinkling of the flame. In the limit that the density gradient is completely isotropic, the PDFs uniformly equal 0.5.

Considering cases A, B, C*, and D, the orientation of the density gradient becomes more isotropic as the Karlovitz number increases and density ratio decreases. In addition, there is a significant increase in the isotropy of the density gradient with a larger value of l/l_F (case B versus $B^4_{Tab,1}$). The greater isotropy of the flame normal (defined as the unit normal aligned with the density gradient) in $B^4_{Tab,1}$ is visually evident when considering Fig. 3 and is due to the larger length scales over which the flame may wrinkle.

D. Discussion

In Section III, it was found that larger values of both the Karlovitz number and large turbulent scales (l/l_F) promote vorticity isotropy. However, they alter the isotropy of the smallest turbulent scale in different ways.

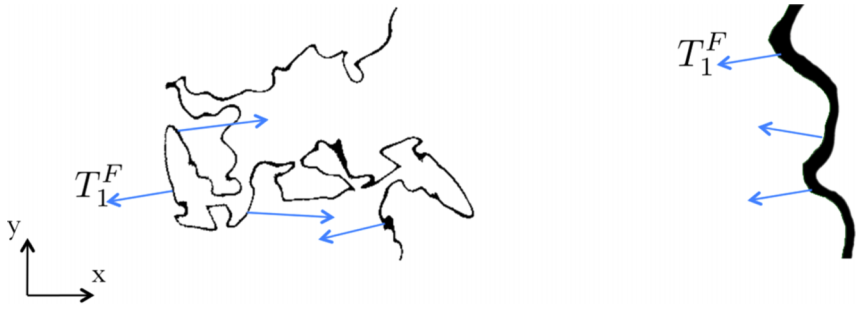

FIG. 15. Illustration of the influence of flame geometry on the resulting anisotropy production. The solid black line represents the flame surface while arrows represents the effect of the flame on vorticity.

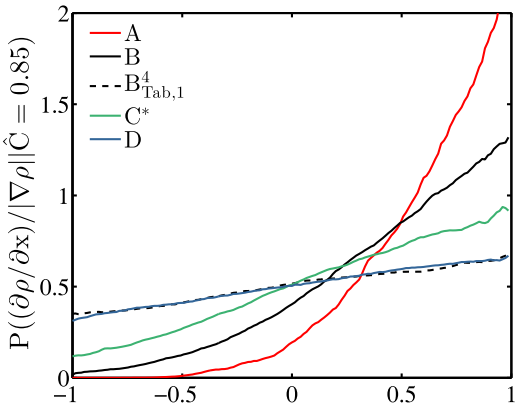

FIG. 16. PDFs of $(\partial\rho/\partial x)/|\nabla\rho|$ for cases A, B, $B^4_{Tab,1}$, C*, and D at $\hat{C} = 0.85$. Values of 1 and −1 represent alignment of the density gradient and the respective coordinate direction, while 0 represents orthogonality.

At sufficiently high Karlovitz numbers, the local dynamics of the vortex stretching term and vorticity vector were found to resemble homogeneous isotropic turbulence (exemplified by case D in Sections IV A and IV B). Small scale isotropy results because of a fundamental similarity in the behavior of the smallest turbulent scales throughout the flame and in homogeneous isotropic turbulence. The Ka and density ratio dependence help explain the increasing isotropy between cases A, B, C*, and D.

This description is illustrated in Fig. 17, which highlights the competing effects of the turbulence and flame on the alignment of vorticity in the strain-rate eigenframe. In the flame, the alignment with the S_1 direction increases at lower Karlovitz numbers, promoting an increase in vortex stretching in S_1 (possibly scaling with Ka/γ). Concurrently, the turbulence attempts to relax the flow towards homogeneous isotropic turbulence with vorticity preferentially aligning with S_2. As written in the figure, vortex stretching (when considered alone) amplifies vorticity, resulting in its exponential growth. Qualitatively, the effects of this mechanism are consistent with the observed behavior of W_x, as λ_1 is the largest positive eigenvalue and vorticity anisotropy demonstrates a compounding growth through the flame (Fig. 4). This is most clearly seen in cases A and B which have the greatest levels of anisotropy.

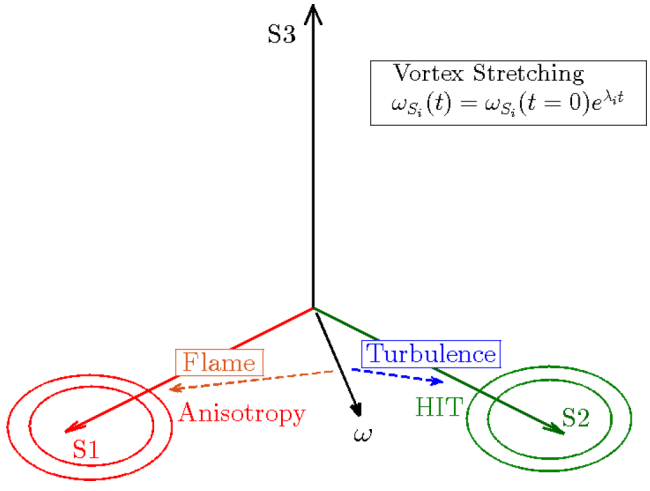

FIG. 17. Illustration of the competition between the flame and the turbulence on the local alignment of vorticity in the strain-rate eigenframe, relaxing the turbulence toward homogeneous isotropic turbulence (HIT) or causing the growth of anisotropy. The quantity ω_{S_i} is the vorticity aligned with the S_i eigenvector and, considering the effects of vortex stretching alone, exponentially grows or decays according to its associated eigenvalue, λ_i.

The local dynamics of vorticity and the vortex stretching term, however, do not explain the greater vorticity isotropy observed in case $B^4_{Tab,1}$ compared to case B (Fig. 4(b)), as the large scales (l/l_F) were found to have minimal impact on their behavior (Figs. 13 and 14). However, greater isotropy of the flame normal in case $B^4_{Tab,1}$ compared with case B (Fig. 16) suggests that the decreased vorticity anisotropy is simply due to the flame altering the vortex stretching term more equally in all directions, thus reducing the net contribution to anisotropy (the different flame geometries are also visually evident in Fig. 3). This a geometric effect only and is expected to be configuration dependent. The resulting small scale isotropy does not reflect a fundamental similarity between the small scale turbulence dynamics in the flame and in homogeneous isotropic turbulence.

In summary, local and global effects are found to depend separately on the Karlovitz number and large turbulent scales. The combination of these effects produces the observed dependence of anisotropy on these parameters.

V. SUMMARY AND CONCLUSION

The isotropy of the smallest turbulent scales in high Karlovitz number premixed flames was studied by considering the vorticity vector and its transport equation. In this study, we analyzed a series of DNS previously performed by Bobbitt *et al.*[6] of high Karlovitz number premixed flames spanning a wide range of conditions. The conclusions are summarized in the following and several points of application are discussed.

Larger values of both the Karlovitz number and l/l_F were found to promote vorticity isotropy. Given a sufficiently high value of the Karlovitz number, the vorticity is isotropic throughout the flame and the behavior of vorticity within the strain-rate tensor eigenframe resembles that of homogeneous isotropic turbulence. This supports the validity of Kolmogorov's hypothesis of local isotropy in this case.

Vorticity anisotropy, at moderate values of Ka, suggests that Kolmogorov's hypothesis of local isotropy is not valid at lower Karlovitz numbers. The primary cause for the growth of anisotropy was determined to be the vortex stretching term. The local dynamics of the vortex stretching term and vorticity were found to depend on the Karlovitz number and flame density ratio. In this case, the vorticity was found to have greater alignment with the most extensive eigenvector of the strain-rate tensor compared with homogeneous isotropic turbulence. This suggests that the flame promotes an increase in vortex stretching.

A larger value of l/l_F was found to have minimal impact on the local dynamics of vorticity and the vortex stretching term. The results suggest that greater vorticity isotropy is simply due to the flame altering the vortex stretching term more equally in all directions, reducing the net contribution to anisotropy. The resulting isotropy does not reflect a fundamental similarity between smallest turbulent scales in the flame with homogeneous isotropic turbulence. This is a geometric effect only and is expected to be configuration dependent. This conclusion is particularly relevant to practical applications which possess larger integral length scales.

Lastly, it was found that using tabulated chemistry with unity Lewis number transport resulted in the same vorticity anisotropy as with a finite-rate chemical model and constant non-unity Lewis numbers, as similarly found previously for the transport of enstrophy.[6] This supports the use of these simplified chemical and transport models in simulations studying the effects of the flame on turbulence. The ability to employ alternative chemical models allows the future study of more complex geometries and larger turbulent Reynolds numbers. It is expected that any differences in the results due to transport models would be most prominent between unity and constant non-unity Lewis numbers, while difference between constant non-unity and mixture-averaged or multicomponent diffusion would be less. This is because the species Lewis numbers vary relatively little through the flame even when using mixture-averaged formulation.[31] Extension of these conclusions to other conditions, such as lean hydrogen/air flames, where thermo-diffusive instabilities occur, is unclear and should be the subject of future work.

The present results may be related to those of Hamlington *et al.*[15] The primary source of anisotropy identified in the current study is similar to the explanation offered in their work, that

being vortex stretching. However, Hamlington *et al.*[15] observed the onset of isotropy at significantly lower Karlovitz numbers than in the current study. The reasons are as follows. Temperature dependent viscosity increases through the flame which reduces the local Karlovitz number. Lower local Karlovitz numbers were shown here to support an increase in flame induced vortex stretching (possibly scaling with Ka/γ). Without the effects of temperature dependent viscosity (absent in an ILES framework with zero molecular viscosity), the local Karlovitz number will be relatively larger and vortex stretching by the flame will be weaker, which will promote isotropy at lower values of Ka_u. This emphasizes the importance of the physical viscosity to correctly capture the behavior of the smallest turbulent scales in premixed turbulent combustion.

ACKNOWLEDGMENTS

This research was supported by the Department of Defense [Air Force Office of Scientific Research] under Award No. FA9550-12-1-0144. Views and opinions of and endorsements by the author(s) do not reflect those of the US Air Force or the Department of Defense. The authors also gratefully acknowledge the support of the ARCS Los Angeles Chapter.

APPENDIX: ANISOTROPIC TRANSPORT TERMS

The terms in the transport equation for the anisotropy vector, $\boldsymbol{W}$, are provided explicitly here. This equation is written as

$$\frac{1}{2}\frac{D\boldsymbol{W}}{Dt} = \boldsymbol{T}_1 + \boldsymbol{T}_2 + \boldsymbol{T}_3 + \boldsymbol{T}_4 + \boldsymbol{T}_5, \tag{A1}$$

where each term on the right hand side is associated with a specific physical process: production/vortex stretching, dilatation, baroclinic torque, viscous dissipation, and forcing, respectively. The anisotropic production term is written as

$$\boldsymbol{T}_{1,i} = \omega_i \boldsymbol{e}_i \cdot S \cdot \boldsymbol{\omega} - \frac{1}{3}\boldsymbol{\omega} \cdot S \cdot \boldsymbol{\omega}, \tag{A2}$$

anisotropic dilatation may be written as

$$\boldsymbol{T}_2 = (-\boldsymbol{W})(\nabla \cdot \boldsymbol{u}), \tag{A3}$$

anisotropic baroclinic torque is written as

$$\boldsymbol{T}_{3,i} = \frac{\omega_i \boldsymbol{e}_i}{\rho^2} \cdot (\nabla\rho \times \nabla P) - \frac{1}{3}\frac{\boldsymbol{\omega}}{\rho^2} \cdot (\nabla\rho \times \nabla P), \tag{A4}$$

anisotropic viscous dissipation is written as

$$\boldsymbol{T}_{4,i} = \omega_i \boldsymbol{e}_i \cdot \nabla \times \frac{\nabla \cdot \tau}{\rho} - \frac{1}{3}\boldsymbol{\omega} \cdot \nabla \times \frac{\nabla \cdot \tau}{\rho}, \tag{A5}$$

and, lastly, anisotropic forcing takes the form

$$\boldsymbol{T}_{5,i} = \omega_i \boldsymbol{e}_i \cdot \nabla \times \frac{\boldsymbol{f}}{\rho} - \frac{1}{3}\boldsymbol{\omega} \cdot \nabla \times \frac{\boldsymbol{f}}{\rho}. \tag{A6}$$

[1] S. B. Pope, *Turbulent Flows* (Cambridge University Press, 2000).
[2] N. Peters, *Turbulent Combustion* (Cambridge University Press, 2000).
[3] A. R. Kerstein, "Linear-eddy modelling of turbulent transport. VII. Finite-rate chemistry and multi-stream mixing," J. Fluid Mech. **240**, 289–313 (1992).
[4] T. Smith and S. Menon, "Model simulations of freely propagating turbulent premixed flames," Symp. (Int.) Combust., [Proc.] **26**, 299–306 (1996).
[5] S. Menon and W. H. Calhoon, Jr., "Subgrid mixing and molecular transport modeling in a reacting shear layer," Symp. (Int.) Combust., [Proc.] **26**, 59–66 (1996).
[6] B. Bobbitt, S. Lapointe, and G. Blanquart, "Vorticity transformation in high Karlovitz number premixed flames," Phys. Fluids **28**, 015101 (2016).
[7] H. Pitsch, "Large-eddy simulation of turbulent combustion," Annu. Rev. Fluid Mech. **38**, 453–482 (2006).

[8] A. Misra and D. I. Pullin, "A vortex-based subgrid stress model for large-eddy simulation," Phys. Fluids **9**, 2443–2454 (1997).
[9] A. J. Aspden, M. S. Day, and J. B. Bell, "Turbulence–flame interactions in lean premixed hydrogen: Transition to the distributed burning regime," J. Fluid Mech. **680**, 287–320 (2011).
[10] A. Y. Poludnenko and E. S. Oran, "The interaction of high-speed turbulence with flames: Global properties and internal flame structure," Combust. Flame **157**, 995–1011 (2010).
[11] B. Savard, B. Bobbitt, and G. Blanquart, "Structure of a high Karlovitz n-C7H16 premixed turbulent flame," Proc. Combust. Inst. **35**, 1377–1384 (2015).
[12] B. Savard and G. Blanquart, "Broken reaction zone and differential diffusion effects in high Karlovitz n-C7H16 premixed turbulent flames," Combust. Flame **162**, 2020–2033 (2015).
[13] S. Lapointe, B. Savard, and G. Blanquart, "Differential diffusion effects, distributed burning, and local extinctions in high Karlovitz premixed flames," Combust. Flame **162**, 3341–3355 (2015).
[14] B. Savard and G. Blanquart, "An a priori model for the effective species Lewis numbers in premixed turbulent flames," Combust. Flame **161**, 1547–1557 (2014).
[15] P. E. Hamlington, A. Y. Poludnenko, and E. S. Oran, "Interactions between turbulence and flames in premixed reacting flows," Phys. Fluids **23**, 125111 (2011).
[16] P. E. Hamlington, A. Y. Poludnenko, and E. S. Oran, "Intermittency in premixed turbulent reacting flows," Phys. Fluids **24**, 075111 (2012).
[17] N. Chakraborty, "Statistics of vorticity alignment with local strain rates in turbulent premixed flames," Eur. J. Mech. - B/Fluids **46**, 201–220 (2014).
[18] N. Chakraborty, M. Katragadda, and R. S. Cant, "Statistics and modelling of turbulent kinetic energy transport in different regimes of premixed combustion," Flow, Turbul. Combust. **87**, 205–235 (2011).
[19] J. Jiménez, A. A. Wray, P. G. Saffman, and R. S. Rogallo, "The structure of intense vorticity in isotropic turbulence," J. Fluid Mech. **255**, 65–90 (1993).
[20] S. C. Morris and J. F. Foss, "Vorticity spectra in high Reynolds number anisotropic turbulence," Phys. Fluids **17**, 088102 (2005).
[21] C. Poulain, N. Mazellier, P. Gervais, Y. Gagne, and C. Baudet, "Spectral vorticity and Lagrangian velocity measurements in turbulent jets," Flow, Turbul. Combust. **72**, 245–271 (2004).
[22] A. Y. Poludnenko, "Pulsating instability and self-acceleration of fast turbulent flames," Phys. Fluids **27**, 014106 (2015).
[23] A. N. Lipatnikov, S. Nishiki, and T. Hasegawa, "A direct numerical simulation study of vorticity transformation in weakly turbulent premixed flames," Phys. Fluids **26**, 105104 (2014).
[24] F. F. Grinstein, L. G. Margolin, and W. J. Rider, *Implicit Large Eddy Simulation* (Cambridge University Press, 2007).
[25] N. Chakraborty, M. Katragadda, and R. S. Cant, "Effects of Lewis number on turbulent kinetic energy transport in premixed flames," Phys. Fluids **23**, 075109 (2011).
[26] C. Rosales and C. Meneveau, "Linear forcing in numerical simulations of isotropic turbulence: Physical space implementations and convergence properties," Phys. Fluids **17**(9), 095106 (2005).
[27] P. L. Carroll and G. Blanquart, "A proposed modification to Lundgren's physical space velocity forcing method for isotropic turbulence," Phys. Fluids **25**(10), 105114 (2013).
[28] A. Majda, *Compressible Fluid Flow and Systems of Conservation Laws in Several Space Variables* (Springer, New York, 1984), Vol. 53, pp. 72–79.
[29] A. Majda and J. Sethian, "The derivation and numerical solution of the equations for zero mach number combustion," Combust. Sci. Technol. **42**, 185–205 (1985).
[30] F. Bisetti, G. Blanquart, M. E. Mueller, and H. Pitsch, "On the formation and early evolution of soot in turbulent nonpremixed flames," Combust. Flame **159**, 317–335 (2012).
[31] N. Burali, S. Lapointe, B. Bobbitt, G. Blanquart, and Y. Xuan, "Assessment of the constant non-unity Lewis number assumption in chemically-reacting flows," Combust. Theory Modell. **20**(4), 632–657 (2016).
[32] O. Desjardins, G. Blanquart, G. Balarac, and H. Pitsch, "High order conservative finite difference scheme for variable density low Mach number turbulent flows," J. Comput. Phys. **227**, 7125–7159 (2008).
[33] B. Savard, Y. Xuan, B. Bobbitt, and G. Blanquart, "A computationally-efficient, semi-implicit, iterative method for the time-integration of reacting flows with stiff chemistry," J. Comput. Phys. **295**, 740–769 (2015).
[34] B. P. Leonard, "A stable and accurate convective modelling procedure based on quadratic upstream interpolation," Comput. Methods Appl. Mech. Eng. **19**, 59–98 (1979).
[35] M. Herrmann, G. Blanquart, and V. Raman, "Flux corrected finite volume scheme for preserving scalar boundedness in reacting large-Eddy simulations," AIAA J. **44**, 2879–2886 (2006).
[36] E. Knudsen and H. Pitsch, "A general flamelet transformation useful for distinguishing between premixed and non-premixed modes of combustion," Combust. Flame **156**, 678–696 (2009).
[37] O. Gicquel, N. Darabiha, and D. Thévenin, "Liminar premixed hydrogen/air counterflow flame simulations using flame prolongation of ILDM with differential diffusion," Proc. Combust. Inst. **28**, 1901–1908 (2000).
[38] J. van Oijen, F. Lammers, and L. de Goey, "Modeling of complex premixed burner systems by using flamelet-generated manifolds," Combust. Flame **127**, 2124–2134 (2001).
[39] J. D. Regele, E. Knudsen, H. Pitsch, and G. Blanquart, "A two-equation model for non-unity Lewis number differential diffusion in lean premixed laminar flames," Combust. Flame **160**, 240–250 (2013).
[40] S. K. Menon, P. A. Boettcher, and G. Blanquart, "Enthalpy based approach to capture heat transfer effects in premixed combustion," Combust. Flame **160**, 1242–1253 (2013).
[41] T. D. Dunstan, N. Swaminathan, K. N. Bray, and R. S. Cant, "Geometrical properties and turbulent flame speed measurements in stationary premixed V-flames using direct numerical simulation," Flow, Turbul. Combust. **87**, 237–259 (2011).
[42] R. Sankaran, E. R. Hawkes, J. H. Chen, T. Lu, and C. K. Law, "Structure of a spatially developing turbulent lean methane–air Bunsen flame," Proc. Combust. Inst. **31**, 1291–1298 (2007).

[43] R. Sankaran, E. R. Hawkes, C. S. Yoo, and J. H. Chen, "Response of flame thickness and propagation speed under intense turbulence in spatially developing lean premixed methane–air jet flames," Combust. Flame **162**, 3294–3306 (2015).
[44] S. Nishiki, T. Hasegawa, R. Borghi, and R. Himeno, "Modeling of flame-generated turbulence based on direct numerical simulation databases," Proc. Combust. Inst. **29**, 2017–2022 (2002).
[45] A. Y. Poludnenko and E. S. Oran, "The interaction of high-speed turbulence with flames: Turbulent flame speed," Combust. Flame **158**, 301–326 (2011).
[46] A. J. Aspden, J. B. Bell, M. S. Day, S. E. Woosley, and M. Zingale, "Turbulence-flame interactions in type ia supernovae," Astrophys. J. **689**, 1173–1185 (2008).
[47] A. Aspden, M. Day, and J. Bell, "Lewis number effects in distributed flames," Proc. Combust. Inst. **33**, 1473–1480 (2011).
[48] C. Higgins, M. Parlange, and C. Meneveau, "Alignment trends of velocity gradients and subgrid-scale fluxes in the turbulent atmospheric boundary layer," Boundary-Layer Meteorol. **109**, 59–83 (2003).
[49] C. W. Higgins, M. B. Parlange, and C. Meneveau, "The heat flux and the temperature gradient in the lower atmosphere," Geophys. Res. Lett. **31**, L22105, doi:10.1029/2004GL020053 (2004).
[50] A. Tsinober, E. Kit, and T. Dracos, "Experimental investigation of the field of velocity gradients in turbulent flows," J. Fluid Mech. **242**, 169–192 (1992).
[51] W. T. Ashurst, A. R. Kerstein, R. M. Kerr, and C. H. Gibson, "Alignment of vorticity and scalar gradient with strain rate in simulated Navier–Stokes turbulence," Phys. Fluids **30**, 2343–2353 (1987).
[52] R. M. Kerr, "Higher-order derivative correlations and the alignment of small-scale structures in isotropic numerical turbulence," J. Fluid Mech. **153**, 31–58 (1985).
[53] G. Gulitski, M. Kholmyansky, W. Kinzelbach, B. Lüthi, A. Tsinober, and S. Yorish, "Velocity and temperature derivatives in high- Reynolds-number turbulent flows in the atmospheric surface layer. III. Temperature and joint statistics of temperature and velocity derivatives," J. Fluid Mech. **589**, 103–123 (2007).
[54] S. Verma and G. Blanquart, "Subfilter scalar-flux vector orientation in homogeneous isotropic turbulence," Phys. Rev. E **89**, 063015 (2014).
[55] P. L. Carroll, S. Verma, and G. Blanquart, "A novel forcing technique to simulate turbulent mixing in a decaying scalar field," Phys. Fluids **25**, 095102 (2013).
[56] F. A. Jaberi, D. Livescu, and C. K. Madnia, "Characteristics of chemically reacting compressible homogeneous turbulence," Phys. Fluids **12**, 1189–1209 (2000).